Preparation of mesoporous titania xerogels under controlled synthesis conditions. Effects of processing in the textural, adsorption and photocatalytic properties

Jose L. Marco-Brown[a†*], Miguel A. Blesa[a,b] and G. J. A. A. Soler-Illia[a,c]

[a]Gerencia de Química, Comisión Nacional de Energía Atómica, Centro Atómico Constituyentes, Av. Gral. Paz 1499 (B1650KNA), San Martín, Buenos Aires, Argentina
[b]Postgraduate School, Universidad Nacional de General San Martin, Peatonal Belgrano 3563, 1° piso, B1650ANQ, San Martin, Buenos Aires, Argentina
[c]Instituto de Nanosistemas, Universidad Nacional de San Martín, Av. 25 de Mayo y Francia, 1650, San Martín, Buenos Aires, Argentina

*Corresponding author.
E-mail addresses: josemarcobrown@gmail.com, joseluis.marcobrown@unsam.edu.ar (J.L.M-B.), miblesa7@gmail.com (M.A.B), gsoler-illia@unsam.edu.ar (G.J.A.A.S-I.).
Present address:
[†]J.L.M-B: Instituto de Investigación e Ingeniería Ambiental (3iA), Escuela de Ciencia y Tecnología, UNSAM, CONICET, 25 de Mayo y Francia (1650) San Martín, Argentina. Phone: +5491121620334

Abstract

A straightforward and potentially scalable procedure based in the Evaporation-Induced Self-Assembly (EISA) method has been used in order to synthesize mesoporous titania (TiO_2) xerogels. The structural, textural and photocatalytic properties of the synthesized materials were determined. The variation of synthesis parameters relative humidity (RH) and temperature, allowed controlling the textural properties of materials that exhibited mesopores with controllable pore and neck diameter distributions in the range of 3-12 nm, large surface area (125 to 161 m^2 g^{-1}) and pore volume values between 0.17 and 0.38 $cm^3 g^{-1}$. Selected area electron diffraction (SAED) and X-ray diffraction (XRD) patterns indicated the presence of anatase phase. The uptake of gallic acid (GA) on these mesoporous powders and Evonik Degussa P25 was measured using Fourier Transform IR (FTIR) spectroscopy. The photocatalytic degradation rates of GA adsorbed on TiO_2 were measured and followed by FTIR. The mesoporous materials showed interesting features including efficient trapping of the adsorbate and good photolytic response. The catalysts were exposed to successive cycles of adsorption/photolysis of GA and a very good performance was observed for the mesoporous anatase samples, leading to efficient, recoverable and reusable photocatalysts.

Keywords: TiO_2, xerogels, textural properties, adsorption, photocatalyst

1. Introduction

Heterogeneous photocatalysis has been explored in many papers as a possible powerful method to destroy organic pollutants both in water and air; the catalyst of choice is anatase-based titania.

The behavior of the photocatalyst in the presence of strongly adsorbing organics is therefore especially important if practical processes are to be developed. Not only the affinity of the surface for the target contaminant is important; the dynamics of adsorption is also relevant. Whereas the former aspect is mainly determined by the chemical composition of the catalyst, the adsorption rates may be largely influenced by morphological factors such as particle size, porosity, tortuosity, etc.

It is well known that TiO_2 has a high affinity for substances possessing carboxylate ($-COO^-$) and/or phenolic hydroxyl ($-OH$) groups. In previous papers, we described the interaction between particulate TiO_2 and catechol [1], several carboxylic [2-11] and hydroxycarboxylic acids [12, 13], including gallic acid [14, 15], in an attempt to describe the characteristics of the adsorption and surface reactivity of natural organic matter (NOM).The main aspects of adsorption equilibrium and kinetics were described, and the behavior of commercial (Degussa P25) and mesoporous titania were compared [16]. It was shown that mesoporous materials with a stable high surface area, controlled mesoporosity and nanocrystalline framework are an interesting option as photocatalysts, featuring a high adsorption capacity, with affinity similar to that of the commercial material. In these studies, the Attenuated Total Reflectance Fourier Transform Infrared (ATR-FTIR) spectroscopy technique was used to follow the surface evolution of a film deposited onto the ATR crystal [11].

A possible interesting option for photocatalytic reactors designed to destroy organic matter is based in the high adsorption capacity of mesoporous titania with controlled mesoporosity, a nanocrystalline framework and stable high surface area. Such a material offers a huge potential in this field, and improved photocatalytic properties are expected for systems that allow both a high pollutant adsorption and an efficient electron transfer at the same time. Moreover, it may be envisaged that adsorption and photocatalytic mineralization may be carried out in successive steps, and not necessarily simultaneously.

Towards this purpose, it is necessary to solve several issues: (1) the development of an adequate technique to synthesize important (i.e. grams) amounts of mesoporous titania controlling textural properties by manipulating synthesis parameters; (2) the demonstration that adsorption kinetics and equilibria are adequate for a pre-photolytic step; (3) avoiding the poisoning of surface sites and consequent loss of catalytic activity [17], aiming at the reuse of the photocatalyst for several cycles of adsorption/photolysis. These are the subjects addressed in this paper.

Several routes have been proposed to synthesize porous TiO_2 spheres or powders, such as structure-directing agents [18], refluxing [19], hydrothermal/solvothermal methods [20], microwave-assisted hydrothermal

reaction of spherical particle precursors followed by annealing in air [21] or via destabilization of ionic-liquid-like precursors [22]. However, large-scale synthesis of porous TiO_2 powders with tunable surface, pore diameter and pore volume remains a challenge.

In this sense, the use of evaporation-induced self-assembly (EISA) process allows the tuning of macroscopic shape (aerosol, monoliths, films and powders), the textural properties (surface, pore diameter, pore volume) as the active phase of the final material [16, 23-27]. In the particular case of non-silica mesoporous materials, the EISA route has the advantage of been more reliable and reproducible than that based on precipitation [16]. The control of macroscopic shape results important due to the potential use of the material in reactors and the possibility of easy recovery of the photocatalyst.

Scientific efforts had been done in preparation of TiO_2 materials in the form of monoliths, microspheres or powders [16, 18, 19, 23, 24, 27] in order to obtain materials presenting highly photoactive nanocrystalline walls that can be easily separated form aqueous medium after their use as heterocatalysts. Separation of micrometer particles with nanocrystalline texture is far easier and inexpensive solution for decantation or flocculation processes.

Gallic acid (GA, 3,4,5-trihydoxybenzoic acid) is one of the simplest phenolic compound commonly present agricultural wastewater and used as a model of natural organic matter (NOM). ATR-FTIR spectroscopy has been successfully used in kinetic studies of compounds adsorption on different solids [11, 28, 29] and can give a clearer understanding of the behavior of GA adsorption in TiO_2 derived materials. In particular, this technique has been proven useful to follow *in situ* the photocatalytic degradation of GA adsorbed on TiO_2 film [11], and an evaluation of the photocatalyst surface poisoning by degradation intermediates or products can be performed.

In this work, we present a detailed study in the synthesis of crystalline mesoporous titania powders derived from xerogels, produced through an EISA process under controlled humidity and temperature conditions. We demonstrate that the textural properties can be tuned by controlling these two synthetic parameters, leading to obtain a highly porous nanocrystalline material that is easily and environmentally handled. In addition, we study the use of these mesoporous titania phases as recoverable adsorbents and photocatalysts in the degradation of GA, a model pollutant.

2. Experimental details

2.1. Materials

Ethanol and titanium tetrachloride were purchased from Merck. Pluronic F127 and gallic acid (3,4,5-trihydroxybenzoic acid, GA) were obtained from Sigma Aldrich. Commercial TiO_2 (Evonik Degussa P25, now offered as Aeroxide P25) was used without further purification, as a reference for the photocatalytic

activity. P25 is composed mainly of anatase (ca. 75%) and rutile (ca. 25%). The modal particle size is ca. 25 nm, but it readily aggregates in water, reaching particles aggregate sizes of the order of 0.1 µm or more [30]; its BET specific area is 51.4 m^2 g^{-1}. Water was purified in an E-pure equipment.

2.2. Synthesis of mesoporous titania

Mesoporous TiO_2 (MT) was prepared by evaporation-induced self-assembly (EISA) method [25]. A 1:40 molar Ti:EtOH stock solution was prepared by dissolving $TiCl_4$ (4.49 g) in ethanol (43.60 g) under vigorous stirring (in an ice-water bath to avoid overheating, contained in a fume hood due to the HCl vapors produced) and was then stored at 25 ºC away from light until used. In a typical synthesis, 0.68 g of the template (nonionic triblock copolymer Pluronics F127, $EO_{106}PO_{70}EO_{106}$) was dissolved in a 20.0 g of the $TiCl_4$-EtOH solution under stirring at 35 ºC and then cooled to 25 ºC. Subsequently, 1.77 g of water was added dropwise while stirring in order to obtain a molar ratio Ti/F127/H_2O/EtOH = 1/0.005/10/40.

The final sol obtained (total mass of 22.45 g) was left to react in a 250 cm^3 double glass-jacketed reactor thermostated by water flux at a pre-fixed temperature. The reactor has a Teflon cap with an inlet connection for the ingress of a smooth air stream and one outlet connection through which the vapors released are discharged and collected in a NaOH solution by bubbling. The air injected into the reactor was previously bubbled through a saturated salt solution or silica gel column for the purpose of controlling the relative humidity (RH). The RH value of the air stream was measured using a hygrometer prior to entering the reactor. This arrangement enabled the control of the synthesis parameters temperature and airflow RH injected into the reactor (see Fig. S.1, supplementary material). Experiments were performed at temperatures of 30, 40, 50 and 70 ºC, and the values of air RH injected were set to 0, 30, 50 and 70 % for each temperature, by passing the air through silica gel column or 200 cm^3 of saturated $MgCl_2 \cdot 6H_2O$, $Ca(NO_3)_2 \cdot 4H_2O$ or $NaNO_3$ solutions respectively (by bubbling).

The obtained MT samples after drying displayed a heterogeneous aspect, presenting white crystalline regions and zones with translucent gel characteristics. Analysis by FTIR of portions of both regions indicated similar organic content from template (not shown).The drying time to obtain the final as-synthesized material varied according to the temperature and RH parameters of synthesis between 1 to 5 days. The time required to complete the synthesis increased with RH value and decreased with the synthesis temperature. Typical synthesis times are shown in Table 1.

As-prepared MT samples were characterized by FTIR; a thermal treatment was performed by heating the material with a ramp of 1 ºC min^{-1} up to 80 ºC maintaining this temperature for 24 h in order to eliminate the remaining solvent. The sample was then heated with a ramp of 1 ºC min^{-1} up to 130 ºC holding this temperature for 20 h followed by a ramp of 1 ºC min^{-1} up to 350 ºC maintaining

this temperature for 3 h. After this thermal treatment, a white powder was obtained.

The thermally treated MT samples were grounded in an agate mortar and sieved with a 150 μm mesh and designated as MTxRHy, where *x* and *y* indicate the synthesis temperature (in degrees Celsius) and the value of RH in the air flux, respectively. In a typical synthesis, *ca.* 0.7 g of mesoporous titania were obtained per 20g of initial Ti(IV) solution after the EISA and calcination steps (ca. 90% yield TiO_2).

2.3. Characterization

Fourier-Transform Infrared Spectra (FTIR) of as-synthesized and MTxRHy samples was performed in order to verify the template elimination by thermal treatment. FTIR spectra were recorded on a Nicolet-IR 560 spectrometer E.S.P. instrument equipped with a liquid nitrogen-cooled MCT-A detector, using KBr discs (256 scans, resolution 2 cm^{-1}).

The X-ray diffraction patterns (XRD), counting time of 10 s/step collected from 10 to 80° (2θ) were obtained using a PANalytical Empyrean instrument equipped with a PIXcel 3D detector. The crystallite size was estimated by applying the Scherrer equation.

Nitrogen adsorption-desorption isotherms were recorded at 77 K using a Micromeritics ASAP 2010 instrument. The specific surface area was calculated using the BET method. The porosity evaluation was done via Barrett-Joyner-Halenda (BJH) models, from the adsorption branch. All samples were degassed at 150 °C for at least 12 hours prior to measurement.

Transmission electron microscopy (TEM) images were recorded using a Philips CM200 Super Twin instrument operated at 160 kV. Powder samples, suspended in absolute ethanol, were deposited on carbon-coated copper grids, and left until complete solvent evaporation.

2.4. Gallic acid adsorption and photocatalytic degradation

The adsorption kinetics of GA on TiO_2 films and the photocatalytic degradation rates of GA adsorbed on TiO_2 were measured as described in previous a work [16]. The ATR-FT-IR measurements were performed in a Nicolet 8700 FTIR spectrometer (200 scans, resolution 4 cm^{-1}) equipped with a liquid N_2 cooled MCT-A detector and a Spectra Tech ZnSe–ATR crystal unit (area = 10 ×72 mm^2) with an incident angle of 45° and 11 reflections.

Thin colloidal films of TiO_2 were deposited on an ATR crystal by spreading 1.000 cm^3 of water suspensions of MTxRHy or P25 (1.2 g dm^{-3}) and allowed to gently evaporate overnight. The TiO_2 films thus formed were then rinsed, first

with water to eliminate loosely deposited particles and afterwards with a 1×10^{-2} mol dm^{-3} KCl solution. Subsequently, 0.600 cm^3 of a 1×10^{-2} mol dm^{-3} KCl solution were added and a blank sample was recorded. After that, a freshly prepared solution of 1.6×10^{-3} mol dm^{-3} GA in 1×10^{-2} mol dm^{-3} KCl was placed onto the TiO_2 film for the purpose of obtain a GA initial concentration of 1.0×10^{-3} mol dm^{-3}. In order to follow GA adsorption, ATR-FTIR spectra were recorded as a function of time at room temperature until no further changes were detected. This indicated that the surface film had been saturated with the adsorbent. Typically, equilibration times were in the order of 100-120 min (48 min for P25). When the spectra showed no more appreciable changes, the ATR cell was emptied and remaining excess solution was gently removed using absorbent paper.

After the solution was removed, a very small amount (0.100 cm^3) of water was added to prevent film cracking, and the system was exposed to a 15 W, 365 nm UV lamp (FL15BLB Black Light Blue, Toshiba) for 5 min. Sequential ATR-IR spectra were recorded after each UV irradiation step to follow the disappearance of the characteristic bands of GA-TiO_2 surface complexes. When no further spectral changes were observed, the ATR cell was emptied. The remaining solution was smoothly removed using absorbent paper. The adsorption/photolysis sequence was repeated several times in order to study the reusability of the adsorbent/catalyst, and to evaluate possible fouling or poisoning.

The action spectrum of the UV lamp is a band centred at 350 nm, with a half-height width of 50 nm [16]. The total radiation incident on the film, measured by chemical actinometry with potassium ferrioxalate [31], was 2.31×10^{16} photons s^{-1}. The IR band area between 1278 and 1140 cm^{-1}, assigned to ν(Ph-O)/OH def vib (COOH monomer) [14] was chosen in order to follow the changes in the GA surface excess.

3. Results and discussion

3.1. Characterization of MT phases

MT samples were grinded after thermal treatment to yield white and fine powders. Template removal was completed when as-synthesized MT samples were thermally treated at 350 ºC, as indicated both by the absence of residual amorphous carbon (calcined samples were white-coloured), as well as the absence of FTIR bands due to C-H groups (see Fig. S.2, supplementary material). This is in agreement with previous results [25].

Typical TEM images of a mesoporous MT samples obtained after thermal treatment are shown in Fig. 1A (MT70RH70 sample) and Fig. S3 (MT50RH70 sample). In all cases, granular materials presenting regular mesopores similar to bicontinuous worm-like mesophases were obtained. This kind of texture has been obtained previously on TiO_2 xerogels using surfactants as templating

agents [32, 33]. Histograms (see inset in Fig. 1A) of grain size diameters (GSD) obtained from analysis of the TEM images are in good agreement with the anatase crystallite size (D_{ANA}) calculated from XRD analysis (see Fig. 1C). Selected area electron diffraction (SAED) patterns of samples also indicate the presence of anatase phase as seen in the inset of Fig. 1A.
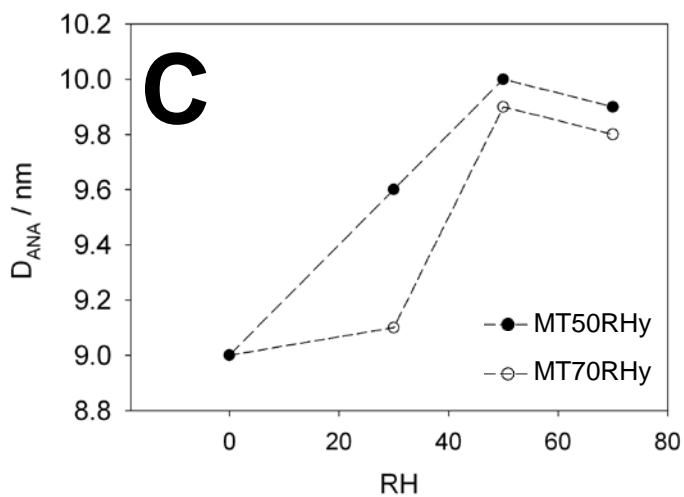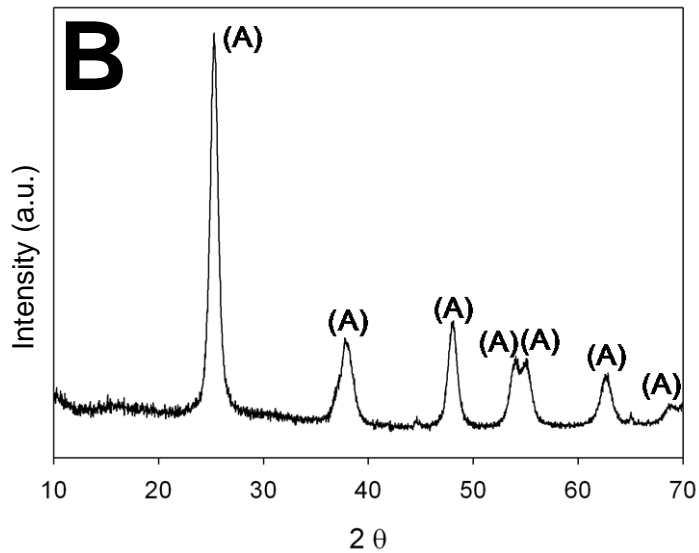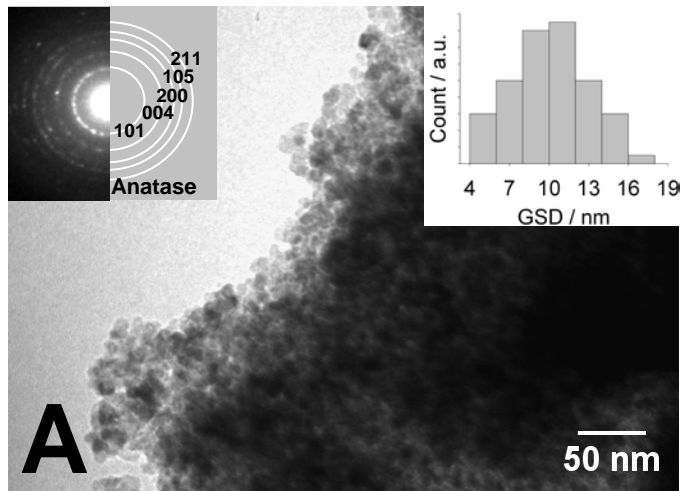
Fig. 1. (A) TEM image of MT70RH70 (insets correspond to grain size diameters (GSD) histograms and SAED pattern). (B) XRD pattern of MT70RH70 sample. Peaks in B corresponded to anatase. (C) Dependence of D_{ANA} on RH for samples obtained after performing EISA at temperatures of 50 and 70°C.

All samples submitted to the 350°C thermal treatment display nanocrystalline walls, as exemplified by the wide-angle diffraction pattern of the MT70RH70 sample presented in Fig. 1B, which was similar to those obtained for other samples (not shown). This result was in excellent agreement with the SAED pattern analysis. The coherently scattering domain (CSD) size, which is related to the average crystallite diameters (D_{ANA}), were calculated from the anatase (101) XRD peak full width at half-maximum using the Scherrer equation; results are reported in Table 1. Crystallite size was not sensitive to the synthesis temperature, but increased slightly with increasing RH (Fig. 1C).

N_2 adsorption-desorption isotherms shown in Fig. 2A and S.4A correspond to typical mesoporous materials. All MTxRHy materials presented type IV nitrogen adsorption-desorption isotherms associated to mesoporosity. Type H2 hysteresis and the existence of percolation processes (closure hysteresis at $P/P_0=0.42$) are characteristic features of materials with interconnected pores [34, 35]. As the RH values, at which samples were synthesized, increased, maintaining the reactor temperature at a constant value, the following main features were observed:

(a) samples presented similar nitrogen adsorption at very low pressure indicating that the microporosity was not very sensitive to changes in RH; very low micropore volume values of less than 0.001 cm^3 g^{-1} were typically obtained,

(b) the overall surface area remained in the same order of magnitude and no clear trends were observed,

(c) the closure of the hysteresis loop take place at the same value of P/P_0; however, the inflection to higher P/P_0 was significantly shifted to larger P/P_0 values, and the gas adsorption values increased, indicating an increase in the mesopore dimension.

It is clear that, at a constant EISA reaction temperature, as the value of RH increased, the mesopore texture was modified; in particular, pore size was enlarged, while only relative minor modifications were observed in the microporosity and surface area.
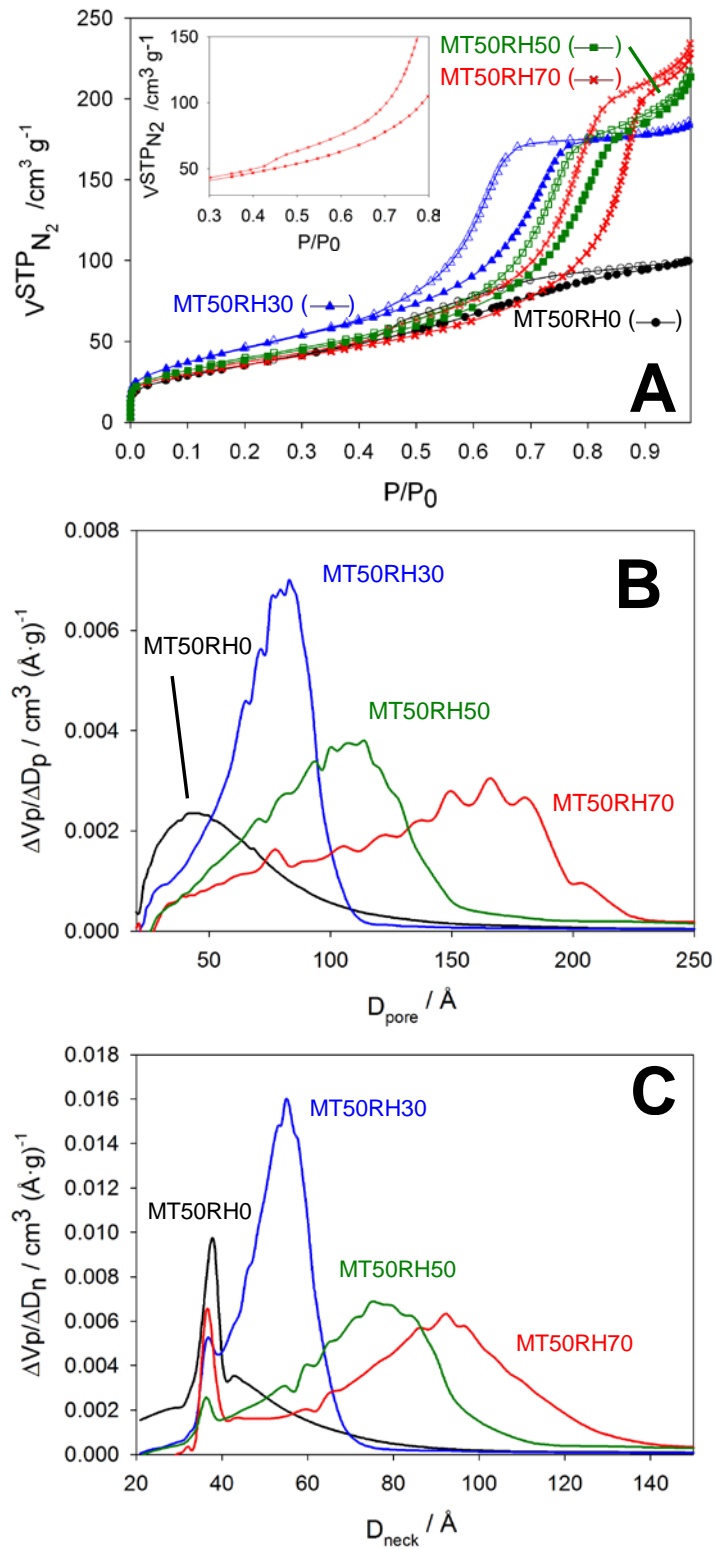
Fig. 2. (A) Nitrogen adsorption isotherms. (B) Pore diameter size distribution (PSD). (C) Neck pore diameter distribution.

Table 1
Porosity and structure characteristics of MTxRHy samples.

sample	synthesis time (days)[a]	surface area (m^2g^{-1})[b]	Pore volume (cm^3g^{-1})[c]	average pore size (nm)[d]	average neck size (nm)[e]	D_{ANA} (nm)
MT30RH0	4	146	0.17	5.6	3.8	8.9
MT40RH0	3	143	0.18	5.9	4.3	8.7
MT50RH0	2	131	0.15	6.7	4.5	9.0
MT50RH30	3	170	0.28	7.7	5.5	9.6
MT50RH50	3	139	0.31	10.6	7.5	10.0
MT50RH70	5	127	0.33	14.7	9.1	9.9
MT70RH0	1	148	0.18	6.2	4.1	9.0
MT70RH30	1	161	0.33	10.1	7.3	9.1
MT70RH50	1	156	0.38	11.7	8.5	9.9
MT70RH70	1	149	0.36	12.1	8.1	9.8
P25[f]		50				25 (R), 80 (A)

[a]Time required to complete the synthesis. [b]BET. [c]Gurvitch. [d]Diameter measuered from the BJH adsorption branch. [e]Diameter measured From the BJH desorption branch. [f]From Araujo et al., 2010 [16].

Table 1 summarizes the structural and textural results obtained. The BET surface areas were of the same order of magnitude (130-170 m^2/g) in all samples treated at 350°C, slightly lower than analogous samples obtained in the case of F127-templated mesoporous titania aerosols [16]. Surface area was slightly higher for RH=30 at both 50 and 70 ºC. The pore diameter size distributions (PSD) in Fig. 2B, S.4B and S.5C were calculated from the adsorption branch of isotherms by the BJH method. An increase in the widening of the PSD was observed with the increase of RH at a constant temperature. At RH=0 no significant changes in the PSD with the EISA temperature were observed. From each distribution, the average pore sizes were calculated and indicated in Table 1. The desorption curves showed a sharp drop corresponding to the capillary evaporation interval. This behaviour has been observed in ink-bottle mesoporous materials [34]. Current models consider that this lower pressure limit can be associated with the size of smallest mesopores that still exhibit adsorption-desorption hysteresis. In cage-like pores, this size correlates well with the mesopore entrances or "interpore necks" [16]. The distributions of neck diameter size calculated from the desorption branch by the BJH method are shown in Fig. 2C, S.4D and S.4E. In all samples a bimodal neck diameter size distribution were observed showing a narrow peak at 3.6-3.7 nm. This narrow peak was attributed to a percolation effect [36]. This percolation effect was clearly observed at P/P_0 values around 0.42 in nitrogen adsorption isotherms (see inset in Fig. 2A corresponding to MT50RH70). The sudden drop in V^{STP}_{N2} resulted from a forced closure of the hysteresis loop around $P/P_0 \sim 0.42$ arising from the tensile strength effect (TSE) of the adsorbed phase [37]. Increases in the widening of neck diameter distributions were observed with the increase of RH at a constant temperature.

At RH=0 there was no significant changes in the neck diameter distributions with temperature. Table 1 also shows the average interpore neck diameters.
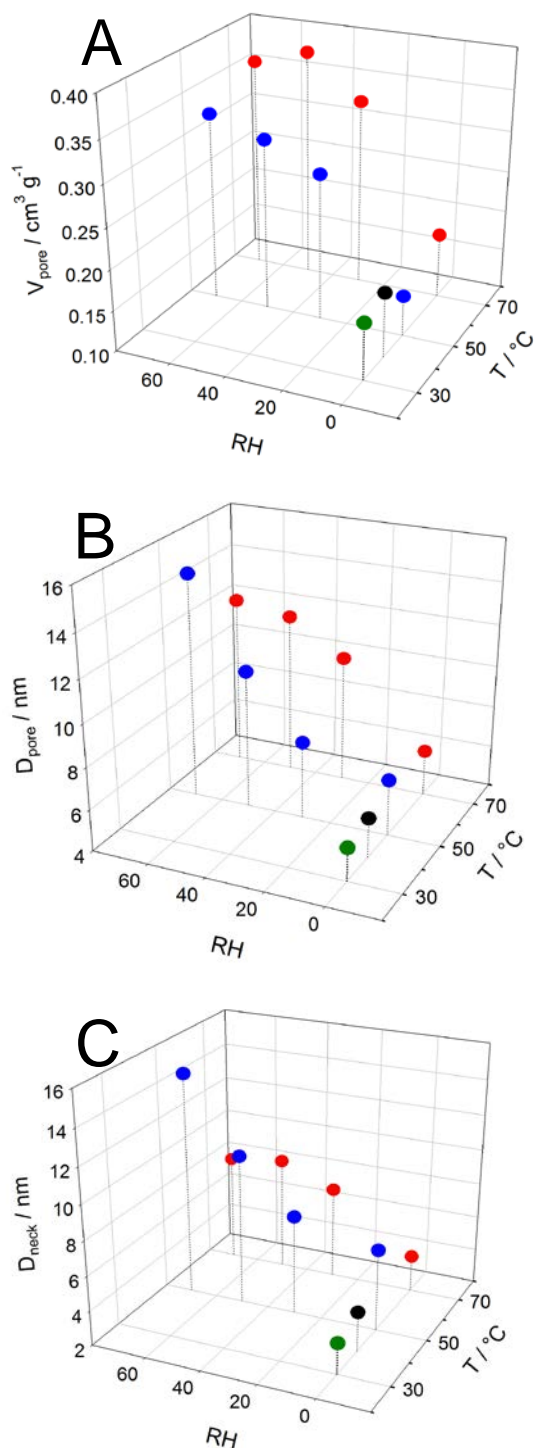

Fig. 3. Dependence of (A) pore volume, (B) average pore diameter and (C) average neck diameter, with synthesis parameters (temperature and RH). Pore volume was calculated by Gurvitch.

The evolution of the D_{ANA}, pore volume, average pore diameter and average neck size with temperature and RH is shown in Fig. 1C, 3A, 3B and 3C, respectively.

Overall, a sustained increase in the pore volume, pore diameter, neck diameter, and D_{ANA} were observed with the increase of RH at a constant EISA temperature. In addition, a widening of pore and neck diameter distribution were also observed for higher RH values at constant temperatures. On the other hand, increasing EISA temperature at RH=0 produced no significant changes in pore volume, neck size, pore size or the pore size distribution. For higher constant RH values, a temperature increase resulted in a slight increase in pore volume. This can be due to an increase in the condensation rate with an increasing temperature, which hardens the mesostructure before complete assembly between the template and the inorganic building blocks. The effect of the EISA temperature in the pore and neck diameters was more subtle. For RH <50%, an increase in temperature resulted in slightly larger pores and necks. The decrease in pore and neck diameter for higher reaction temperature with samples produced at RH=70% suggests that at these higher water contents, a certain swelling of the mesophase take place first, as already observed in freshly prepared, uncondensed mesostructured titania thin films. Drying at higher temperatures could resulted in some extended shrinkage of the inorganic walls, therefore explaining the smaller pore size values observed.

These results indicated that the structural and textural characteristics of MTxRHy samples seem to depend mostly of the changes in RH during the synthesis. This reinforces the general observation that water content is essential during the evaporation phase of the EISA synthesis, as was observed in the case of mesoporous titania thin films [38], and a number of systems [37, 39, 40]. An increase of RH induces a slower solvent evaporation. This, in turn, keeps the inorganic polymerization rate slow, by locally increasing the HCl concentration, which affects the organization of the final material. This is in agreement with the dependency of the time required to complete the synthesis with RH and temperature values (vide supra). The time required to complete the synthesis increased with the RH value and decreased with the reaction temperature. The RH dependence in the final characteristics of mesoporous TiO_2 synthesis was extendedly studied before [38]. Higher values of RH permit to keep a liquid-like soft hybrid mesophase for longer times, leading to a better phase separation of the template. It has been proposed that the presence of water at high values of RH facilitates the organization of the meso-structure in titania thin films [39]. This leads to larger mesopores and more developed interpore necks.

Recently, Herregods et al., concluded from a study of the synthesis of mesoporous titania via EISA and using Brij 58 as template, that temperature does have an important influence in the specific surface area and total volume in the range between 60 and 120°C [37]. Authors attributed this effect to the growth of anatase nanocrystals along this low temperature thermal treatment that might disrupt self-assembly [37]. The reaction conditions in this work are somewhat different, due to the RH was kept constant. This parameter

influenced the dynamics of phase separation and assembly, because the presence of higher water contents in the mesophase could assisted the rearrangement of the template, and an optimization of the interactions at the hybrid interface.

The synthesis proposed in this work allows the reproducible and controlled production of mesoporous titania powders at a scale of grams per day, being able to primarily control the pore size, pore volume and crystallite diameter of the material. The control of these structural characteristics has been achieved by varying RH and temperature, which were central parameters of synthesis. A clear dependence of the textural characteristics with RH was observed: higher RH values permitted to keep fluidity in the mesophase and leaded to larger, accessible mesoporosity.

The use of mesoporous nanocrystalline titania in photocatalytic processes is promising. In this regard an analysis of the use of the materials synthesized in the adsorption and photocatalysis of gallic acid was performed, which will be presented in the next section.

3.2. Gallic acid adsorption and photocatalytic degradation

Adsorption of the model pollutant gallic acid (GA) onto MTxRHy films from a solution containing [GA] =1 × 10^{-3} mol dm^{-3} at pH 3.5 in 1 × 10^{-2} mol dm^{-3} KCl was completed in about 1 h; GA adsorption on P25 in the same conditions occurred in about 30 min. Fig. 4A shows a typical FTIR spectrum of GA adsorbed on films made up of MTxRHy particles deposited on an ATR crystal (see Experimental). The peaks at 1500, 1440, 1358, 1230 and 1070 cm^{-1} have been assigned before [14] to ν(-C=C-)/ν(-C-C-), C-O str plus O-H, δ(Ph-O-H/C-O), ν(Ph-O)/OH def vib (COOH monomer) and δ(C-H) in plane, respectively. Fig. 4B and 4C show the time evolution of the peak centered at 1230 cm^{-1} for adsorption and photolysis experiments respectively. This peak was selected and used to follow adsorption and photolysis kinetics due to its strong molar extinction coefficient (ε). Peaks at 1358 and 1070 cm^{-1} had a smaller ε value. The corresponding band varied monotonously, without changing its shape; thus, no indication of possible accumulation of intermediates was apparent after the analysis of the spectral data.
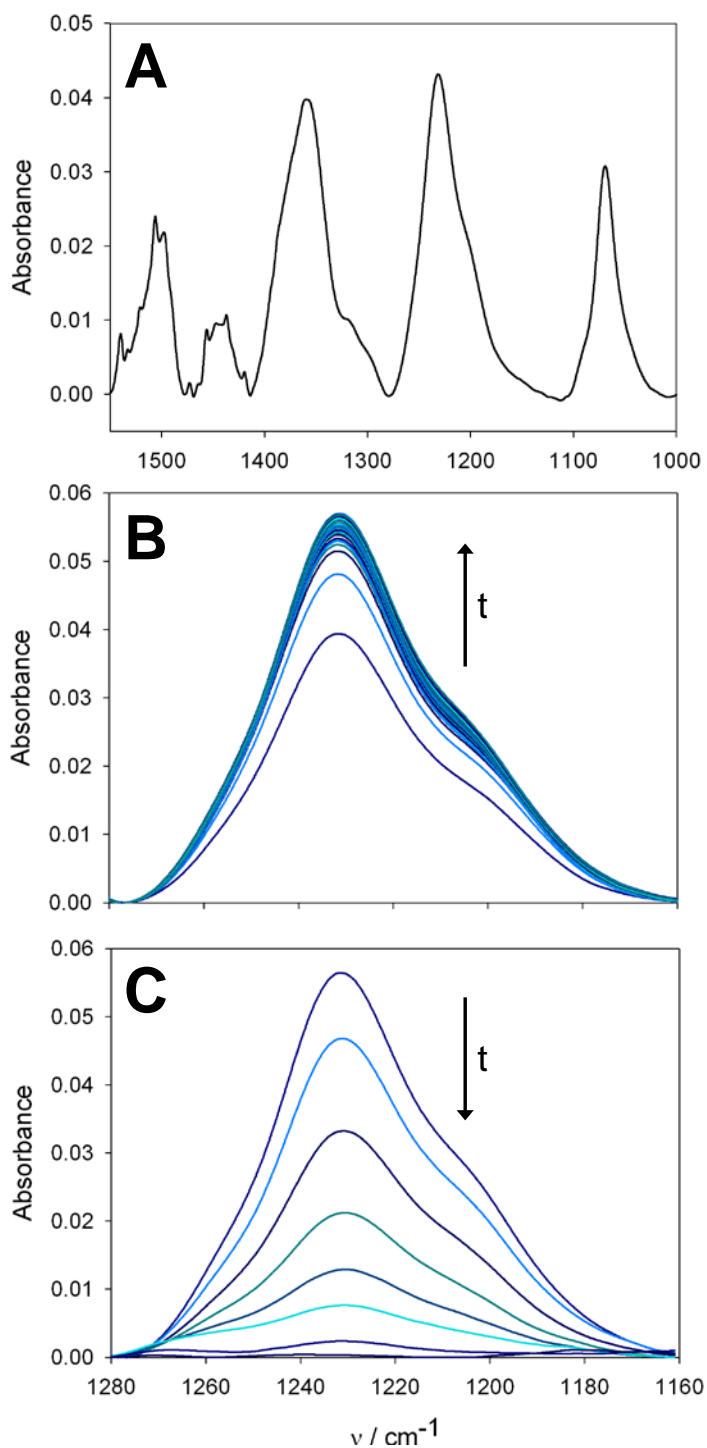
Fig. 4. (A) Region of FTIR spectrum corresponding to GA adsorbed on TiO_2 films. (B) Time evolution of the carboxylate peak at 1230 cm^{-1} in a typical adsorption kinetic experiment. (C) Time evolution of the 1230 cm^{-1} peak in a typical photolysis experiment. (Figures correspond to the MT70RH70 sample).

Fig. 5 shows the time evolution of the band area centred at 1230 cm^{-1} for comparable masses of MTxRHy and P25 samples. The data are plotted in terms of the time evolution of the degree of surface coverage, θ_t, measured as

the ratio A/A_e, where A corresponds to the band area at a given time and A_e corresponds to the band area at long times, when no further appreciable changes in absorbance were detected, e.g. 114 or 48 min for MTxRHy or P25 samples, respectively. The times to obtain the surface coverage θ_e were in line with those found in the adsorption kinetics study of GA on mesoporous TiO_2 microspheres previously reported [16]. The time evolution of θ_t was found to be very reproducible, although the adsorption capacity showed fairly large variations for individual experiments. This latter feature has been attributed to random changes in the fraction of the film that was actually available for adsorption [16].
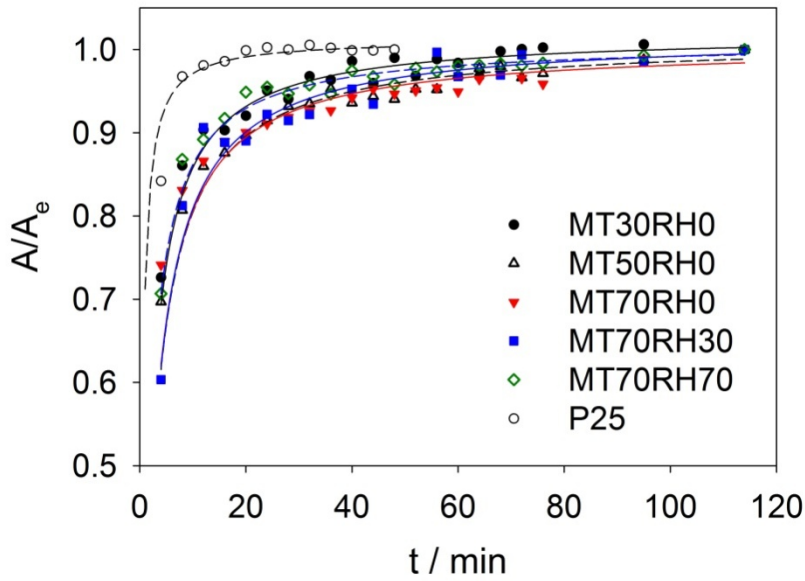

Fig. 5. Time evolution of the band area centred at 1230 cm^{-1}. Traces represent the pseudo-second-order model.

Several kinetic models including Lagergren pseudo-first-order (PFO), pseudo-second-order (PSO) and intra-particle diffusion model (IDM) [29, 41-43] were tested for simulation of the experimental data.

PFO and PSO are used for modeling adsorption kinetics when the overall sorption rate is controlled by the rate of surface reaction, while IDM is applicable when the rate-determining step is the mass transfer of adsorbate to the solid surface sites.

The experimental data did not fitted PFO model (results not shown) but were well described by the empirical pseudo-second-order model which assumes that the adsorption rate is proportional to the square of the number of unoccupied surface sites. Moreover, the number of occupied sites is proportional to the adsorbate concentration. PSO model is defined by Eq. (1), the integrated form being given in Eq. (2).

$$d\theta_t/dt = k_{ad}(\theta_e - \theta_t)^2 \qquad (1)$$

$$t/\theta_t = 1/(k_{ad}\,\theta_e{}^2) + t/\theta_e \qquad\qquad (2)$$

Where θ_e (A_e/A_e) and θ_t (A/A_e) are related to the amount of GA adsorbed at equilibrium and at a given time t, respectively, and k_{ad} is the rate constant of sorption.

The values of $\theta_e k_{ad}$ obtained from the pseudo-second-order equation (Eq. 2) are given in Table 2. As mentioned above, a very good agreement between the experimental data and the pseudo-second-order equation (Eq. 2) was achieved, as indicated by R^2 values in parenthesis, indicating that the mechanism of GA adsorption on MTxRHy synthesized materials was mainly rate-controlled by surface adsorption. MTxRHy samples presented similar $\theta_e k_{ad}$ values, indicating that the GA adsorption mechanism would not depend on the MTxRHy sample, at least in this first analysis.

The $\theta_e k_{ad}$ value of P25 sample was, at least, four times greater than MTxRHy samples, as seen in Table 2. The P25 film was formed of particles that consist of aggregates of 21 nm diameter nanoparticles. An estimated value of pore size of 19 nm for the P25 films was reported previously [11]. It should be relatively easier for reactant molecules to navigate within the aggregated P25 particle mass than through a tortuous mesoporous network of particles with diameters of several hundreds of nanometers to micrometers. Indeed, GA adsorption on MTxRHy samples could take place in the external surface sites of the adsorbent (i.e., those closer to the solution) in a first step, and then GA molecule can enter to the mesoporous network in a second step, as discussed below. Thus, the GA global adsorption-rate on MTxRHy samples was appreciably slowed down when compared to Evonik Degussa P25.

Table 2
PSO and IDM parameters of GA adsorption kinetic on MTxRHy samples obtained by adjusting experimental data by Eq. 2 and 4, resp.

Sample	PSO	IDM	
	$\theta_e k_{ads}$ (min^{-1})	$k_{id}\theta_e{}^{-1}$ (min$^{-1/2}$) $\times 10^{-2}$	C
MT30RH0	0.5±0.1 (0.9996)[a]	1.76±0.04 (0.7618)	0.81±0.05
MT50RH0	0.4±0.1 (0.9996)	2.45±0.03 (0.8656)	0.78±0.04
MT70RH0	0.4±0.1 (0.9994)	2.07±0.02 (0.9961)	0.79±0.03
MT70RH30	0.4±0.1 (0.9986)	2.68±0.03 (0.9408)	0.72±0.04
MT70RH70	0.6±0.1 (0.9998)	3.83±0.02 (0.9626)	0.74±0.03
P25	2.4±0.8 (0.9999)		

[a]Numbers in parenthesis correspond to R^2 values.

Rudzinski and Plazinski [44], traced second order empirical equations to a two-site adsorption process. The formation of inner sphere complexes of GA and salicylate through the interaction of two of their adjacent OH groups with one centre site of Ti or with two adjacent Ti centres had been proposed previously [13, 14]. In this sense, the adsorption of GA on the TiO_2 surface could occur through the formation of surface complexes by an interaction of GA through two of its adjacent OH groups with $\sim_\nu TiOH^{1/3-}$ and $>OH^{1/3+}$ TiO_2 (anatase) sites (See Fig. S.5, supplementary material).

Although a good adjustment of experimental data to PSO model was obtained, a diffusion mechanism may contribute to the rate-controlling step of adsorption [29] and the results obtained using the pseudo-second-order model are not enough to predict the diffusion mechanism [45]. Therefore, the IDM model was investigated to analyse the adsorption kinetic data, in order to evaluate the existence of a diffusional process contribution to the global rate-control due to the effect of the GA molecule entrance into the mesoporous network of MTxRHy samples.

The intraparticle diffusion model (IDM) is applicable when the rate-determining step is the mass transfer of adsorbate to the solid surface sites. The IDM was originally proposed by Boyd in 1947 [46], and is described by Eq. 3

$$\frac{\theta_t}{\theta_e} = 1 - \frac{6}{\pi^2} \sum_{n=1}^{\infty} \frac{1}{n^2} \exp\left(-\frac{Dn^2\pi^2}{r^2}t\right) \qquad (3)$$

where D is the intraparticle diffusion coefficient and r is the particle radius. The Eq. 3 can be simplified to

$$\theta_t = k_{id}\sqrt{t} + C \qquad (4)$$

where k_{id} is the intraparticle diffusion constant, and C is the intercept of the linear plots. If the intraparticle diffusion is the only rate-limiting step, the linear plot of A/A_e versus $t^{1/2}$ should pass through the origin. But, if the intercept C of plots is not equal to zero, the intraparticle diffusion is not the sole rate-determining step.

Plots of A/A_e at 1230 cm^{-1} versus $t^{1/2}$ for GA adsorption on MTxRHy films are shown in Fig. 6.
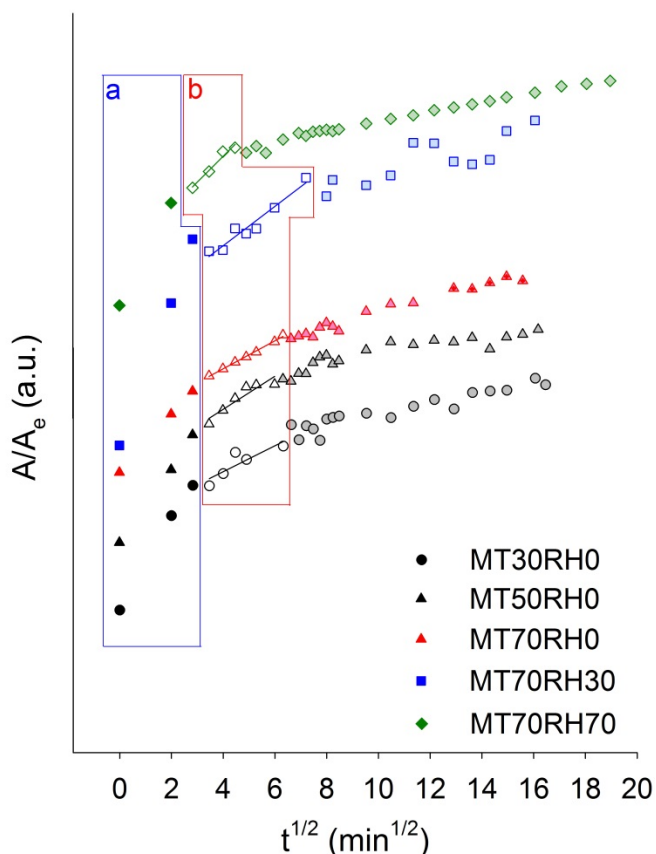
Fig. 6. Plot of A/A_e versus $t^{1/2}$ for MTxRHy samples. Plots have been displaced vertically for a better comprehension. Full filled dots are related to the adsorption on external surface (square area *a*). Empty dots are related to intraparticle diffusion stage (square area *b*) and its linear regression was used to determine $k_{id}\theta_e^{-1}$ and C values by Eq. 4. Semi-empty dots at final times correspond to the final equilibrium stage.

The diffusion kinetics plots (Fig. 6) exhibited the three-stage linearity [47, 48]. The first linear region has been related to high adsorption rate on external surface of the adsorbent (see square area *a* in Fig. 6), which has enough available adsorption sites. Afterwards, while external surface sites are reaching saturation, the GA molecule comes across a much larger diffusion hindrance because of transfer in the deeper inner pores of MTxRHy (see square area *b* in Fig. 6). Finally, the third section was the final equilibrium stage, where the intraparticle diffusion started to slow down due to the low remnant GA concentration in the solution [49]. The ratio between intraparticle diffusion rate k_{id} and θ_e ($k_{id}\theta_e^{-1}$) and C were obtained from the slope and intercept from the linear regression of the second portion of the curve [50] according to the Eq. 4, respectively and presented in Table 2. In addition, the curves did not intercept the origin, indicating that diffusion through the pores is not the limiting factor [45]. These results indicated that intraparticle diffusion dominated in the pore diffusion stage while boundary layer control process played an important role

affecting GA adsorption. This suggests that the adsorption process is complex, and might involve both surface adsorption and intraparticle diffusion [47, 51].

The driving force of diffusion determined by the k_{id} value is very important for adsorption processes on porous materials. The calculated intraparticle diffusion coefficients k_{id} related to θ_e ($k_{id}\theta_e^{-1}$) values for MTxRHy systems are given in Table 2. An increase of average pore size leaded to an increase in the $k_{id}\theta_e^{-1}$ value, indicating that the diffusion of GA molecules into the mesopores depended on the pore size of MTxRHy samples. Larger pore size makes possible an easiest entrance of GA molecules into the mesopore gallery of the particles. On the other hand, the C value reflects the boundary layer effect. As seen in Table 2, there was no significant difference in the C values of the analyzed MTxRHy samples, indicating a similar contribution of the surface sorption in the rate-limiting step, as was indicated by modelling the experimental data by PSO model. Therefore, the double nature of intraparticle diffusion plot confirmed the presence of both surface adsorption and intraparticle diffusion [50].

Summarizing, the GA adsorption on MTxRHy samples was controlled by two kinds of process. At initial times, the GA adsorption occurred at external surface sites and when these sites become saturated, diffusion of GA into the mesoporous gallery occurred. The diffusion-rate depended on the pore size, and an easiest GA diffusion was obtained for larger pores. These results confirmed the importance in the adequate control of the pore systems, in order to control the transport of reagents and products.

The time span required to saturate the film surface is typical of adsorption onto TiO_2 films and describes one of the important limitations of supported film-based photocatalytic reactors as SOLWATER [16]. However, the use of these materials is promising as photocatalytic systems based on adsorption beds in which a first stage the contaminant is removed by adsorption and in a second stage it is photo-degraded. The particle size also allows easy removal by filtration, decantation or flocculation after being used in suspension systems or slurries. P25 on the other hand, being an aggregate of nanoparticles, may release smaller particles, difficult to separate by sedimentation or even filtration.

3.3. Photocatalytic performance and reuse of TiO₂ by in situ regeneration

One of the main pillars for the development of new and more efficient methods of remediation of contaminated aquatic systems is the design of materials that are able to remove the pollutant quickly, easily, and cost-effectively. Ideally, these materials should be easy to remove from the body of water. It will be even more helpful if the material can be recycled for reuse.

In order to estimate the potential of reusing of the solids synthesized and compared with P25, the mesoporous TiO_2 particle films were exposed to successive cycles of GA adsorption followed by photolysis. As was explained in *Section 2.4*, after GA adsorption, the titania materials were irradiated with UV light in order to evaluate the GA photodegradation. The adsorption/photolysis

sequence was repeated five times in order to study the reusability of the adsorbent/catalyst (e.g. 1st GA adsorption was followed by 1st GA photodegradation and the latter was followed by 2nd GA adsorption and so on). Upon exposure to UV light, the intensity of the spectra of the adsorbed GA decreased monotonously with each adsorption/photolysis cycle, without indication of the formation of new species on the surface (Fig. 4C); as was explained before, the FTIR bands of adsorbed GA varies monotonous, without changing its shape indicating that a possible accumulation of intermediates did not occur. A detailed analysis of the mechanism of GA photomineralization is underway, and shall be published separately.

Fig. S.6 shows the plots of the adsorption kinetics and their respective pseudo-second-order adjustments. The kinetic relation $\theta_e k_{ad}$ obtained by Eq. 2 decreased as indicated in Table 3, both for our mesoporous samples and for P25. A marked decrease after the first cycle is followed by an approximate constancy in the case of the mesoporous samples, whereas a gradual decrease is observed in all cycles of the P25 material. There was not enough evidence to interpret the origin of this effect; some early blocking of pores may be involved in the mesoporous samples, and changes in the structure of the adsorption sites may operate in all cases.

Table 3

Parameter $\theta_e k_{ad}$ (min^{-1}) obtained by PSO model (Eq. 2) for GA adsorption kinetic on MTxRHy samples in each adsorption/photolysis sequence

	MT70RH0	MT70RH70	P25
1st	0.4±0.1 (0.9994)[a]	0.6±0.1 (0.9998)	2.4±0.8 (0.9999)
2nd	0.19±0.05 (0.9983)	0.45±0.05 (0.9999)	2.1±0.7 (0.9999)
3rd	0.24±0.04 (0.9994)	0.38±0.05 (0.9998)	1.9±0.5 (0.9999)
4th	0.24±0.05 (0.9990)	0.38±0.05 (0.9998)	1.4±0.3 (0.9999)
5th	0.18±0.04 (0.9988)	0.38±0.05 (0.9999)	1.3±0.3 (0.9999)

[a]Numbers in parenthesis correspond to R^2 values.

Fig. 7 compares the time evolution of the GA FTIR signals for MTxRHy and Degussa P25 during heterogeneous photooxidation. The data showed that the total decomposition of GA in the first cycle or adsorption/photolysis was observed within 30 min for MTxRHy samples and 15 min for P25. As discussed below, the time for total decomposition of GA decreased with successive cycles.
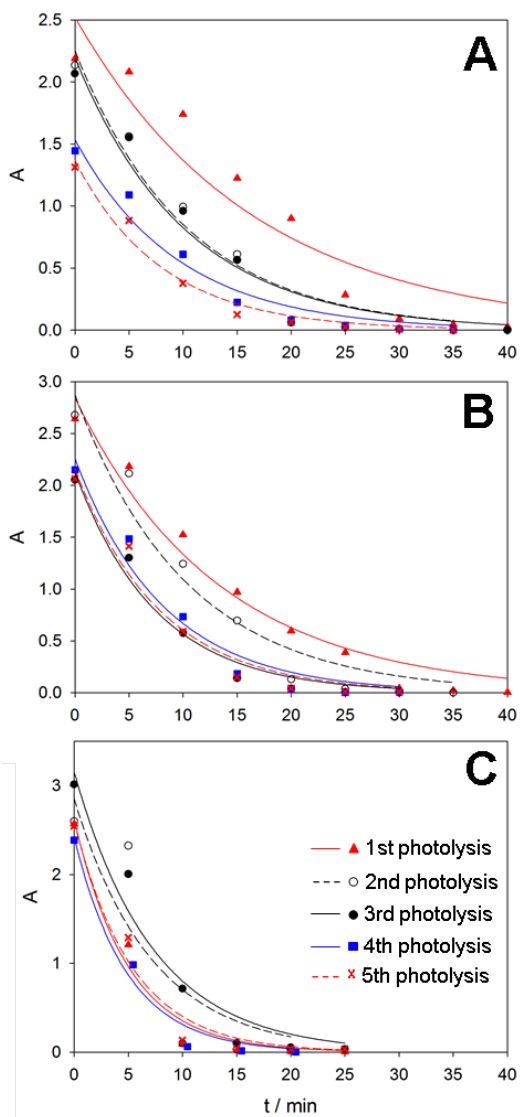
Fig. 7. Time evolution of the integrated area of interest during UV-light illumination of films prepared from (A) MT70RH0, (B) MT70RH70 and (C) P25. Traces correspond to a pseudo-first-order decay adjustment.

The photolytic decay of GA adsorbed was modelled using Eq. 5 corresponding to a pseudo-first-order decay. Calculated parameters are indicated in Table 4 and traced in Fig. 7.

$$A = A_0 \exp(-k_{phot} \, t) \qquad (5)$$

A difference between mesoporous titania and P25 was observed in the behaviour of k_{phot} in the successive cycles; whereas it increased for both MT70RH0 and MT70R70, it remained basically constant for P25, see Fig. 8.

The use of these catalysts in processes for the remediation of contaminated water can be conceived, due to the intrinsic cost of the process, only in cases where the catalyst can be reused in successive treatments. The fact that the adsorption and photocatalytic properties of solids are not deteriorated over time

is an important factor to consider. Any optimization of these parameters for subsequent use of the catalyst leads to an improvement of the process and a reduction in costs. For any practical attempt of use of these catalysts, the improved behaviour in successive cycles is an important feature.

A comparison of the adsorption and photocatalytic performance of the presented mesoporous materials and commercial P25 did not indicate significant advantages for the former. However, the mesoporous material presents four clear improvements over typical limitations of a nanoparticle dispersion such as P25: (a) the porosity and hence the surface area are maintained, avoiding loss in the effective active surface due to aggregation; (b) the larger particle size permits to optimize the catalyst removal from the liquid media to be treated. In this sense, MTxRHy are easiest to remove or separate from a liquid phase than commercial Evonik Degussa P25; (c) the larger surface areas typical of mesoporous TiO_2 provide a higher quantity of active sites and consequently, i.e., higher sensitivity in the development of sensors and (d) the synthesis method explored permits the tuning of pore size, pore volume and anatase crystallite diameters which would be very important in adsorption and catalysis processes.

In addition, the low temperature synthesis procedures offer the possibility to increase cristallinity through a higher thermal treatment, or to incorporate dopants, maintaining at the same time an adequate control of the main morphological and textural features (i.e., pore volume, surface area, D_{ANA}). For example, mesoporous TiO_2 with high surface area, as the one obtained in the present work, has been proved successfully as sensing material for acetone [52]. It has been observed that for mesoporous titania aerosols, larger crystallite sizes result in significantly improved photocatalysis, although a large decrease of surface area took place [16]. Furthermore, dopants can be easily introduced in order to enhance the production of visible light active materials, through the incorporation of metal, nitrogen or others [53, 54]. On the other hand, in synthesis of materials for dye-sensitized solar cells fabrication, a high specific surface area, fast electron transport and large light scattering effect are the desirable properties of photoelectrodes, making possible the use of mesoporous titania instead of P25.

Table 4
Values of k_{phot} calculated using pseudo-first-order photolysis decay for GA photodegradation in each adsorption/photolysis cycle.

		MT70RH0	MT70RH70	P25
1st	A_0	2.5±0.2	2.8±0.2	2.6±0.2
	k_{phot} (min^{-1})	0.06±0.01	0.076±0.007	0.20±0.03
		(0.9083)[a]	(0.9693)	(0.9740)
2nd	A_0	2.3±0.2	2.9±0.2	2.9±0.7
	k_{phot}(min^{-1})	0.10±0.01	0.10±0.01	0.14±0.06
		(0.9599)	(0.9560)	(0.8037)
3rd	A_0	2.2±0.2	2.1±0.1	3.2±0.3

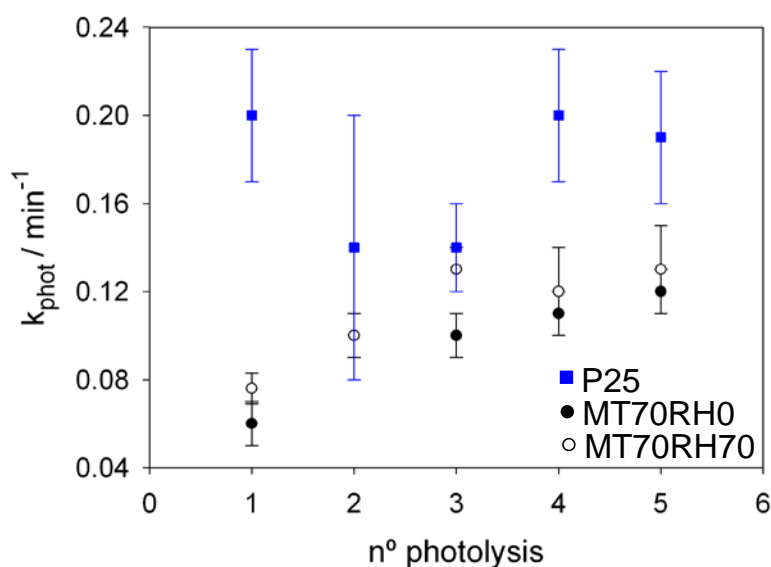|				
	k_{phot}(min^{-1})	0.10±0.01 (0.9614)	0.13±0.02 (0.9767)	0.14±0.02 (0.9592)
4th	A_0	1.5±0.1	2.3±0.2	2.4±0.2
	k_{phot}(min^{-1})	0.11±0.01 (0.9648)	0.12±0.02 (0.9644)	0.20±0.03 (0.9777)
5th	A_0	1.37±0.08	2.2±0.2	2.6±0.2
	k_{phot}(min^{-1})	0.12±0.01 (0.9779)	0.13±0.02 (0.9660)	0.19±0.03 (0.9705)

[a]Numbers in parenthesis correspond to R^2 values.

Fig. 8. Variation of k_{phot} with number of photolysis cycle.

4. Conclusions

A straightforward and potentially scalable procedure to synthesize mesoporous titania has been employed. Parameters of synthesis RH and temperature were explored indicating that RH has the most important effect in controlling textural properties. A systematic increase in the pore volume, pore diameter, neck diameter, and crystallite diameter were observed with the increase of RH at a constant synthesis temperature. In addition, a widening of pore and neck diameter distribution were also observed for higher RH values at constant temperatures. On the other hand, increasing EISA temperature at RH=0 produced no significant changes in pore volume, neck size, pore size or the pore size distribution. For higher constant RH values, a temperature increase resulted in a slight increase in pore volume.

In addition, a clear relationship was found between the adsorption kinetics of GA with the textural properties, especially with pore size. The presence of both

surface adsorption and intraparticle diffusion was confirmed. Larger pore size makes possible an easiest entrance of GA molecules into the mesopore gallery of the particles. A similar contribution of the surface sorption in the rate-limiting step was obtained for all samples.

GA adsorption/photolysis cycles were studied and in principle, both mesoporous titania and commercial Evonik Degussa P25 may be used as a basis for a process in which adsorption and photolysis are separate stages. A comparison of the adsorption and photocatalytic performance of the studied mesoporous materials and P25 did not indicate significant advantages for the former. However, the mesoporous material presented clear improvements over P25, in particular regarding the ease of material recovery.

The organic model pollutant (galic acid) was destroyed by irradiation under moist air, and, indeed at least five cycles were carried out with only small loss of activity. A further improvement in the process can be envisaged by treating the surface with hydrogen peroxide after a few cycles, to clean the surface of the adsorbent/catalyst, extending its lifetime. This strategy is being currently explored.

Thus, the mesoporous material presented here combines a very good performance in adsorption and photolysis, while being able to be presented as easily recoverable micronic or submicronic powders with accessible inner surface

Supplementary material
Supplementary data associated with this article can be found, in the online version, at Colloids and Surfaces A: Physicochemical and Engineering Aspects.

References

[1]   R. Rodríguez, M.A. Blesa, A.E. Regazzoni, Surface complexation at the TiO2 (anatase)/aqueous solution interface: Chemisorption of catechol, J. Colloid Interf. Sci. 177 (1996) 122. http://dx.doi.org/10.1006/jcis.1996.0012

[2]   A.D. Weisz, A.E. Regazzoni, M.A. Blesa, ATR-FTIR study of the stability trends of carboxylate complexes formed on the surface of titanium dioxide particles immersed in water, Solid State Ion. 143 (2001) 125. http://dx.doi.org/10.1016/S0167-2738(01)00840-2

[3]   C.B. Mendive, D.W. Bahnemann, M.A. Blesa, Microscopic characterization of the photocatalytic oxidation of oxalic acid adsorbed onto TiO2 by FTIR-ATR, Catal. Today 101 (2005) 237. http://dx.doi.org/10.1016/j.cattod.2005.03.016

[4]   C.B. Mendive, M.A. Blesa, D. Bahnemann, The adsorption and photodegradation of oxalic acid at the TiO2 surface, Water Sci. Technol. 55 (2007) 139. http://dx.doi.org/10.2166/wst.2007.398

[5]   C.B. Mendive, T. Bredow, M.A. Blesa, D.W. Bahnemann, ATR-FTIR measurements and quantum chemical calculations concerning the adsorption and photoreaction of oxalic acid on TiO2, Phys. Chem. Chem. Phys. 8 (2006) 3232. http://dx.doi.org/10.1039/B518007B

[6]   C.B. Mendive, T. Bredow, A. Feldhoff, M. Blesa, D. Bahnemann, Adsorption of oxalate on rutile particles in aqueous solutions: A spectroscopic, electron-microscopic and theoretical study, Phys. Chem. Chem. Phys. 10 (2008) 1960. http://dx.doi.org/10.1039/B800140P

[7]   C.B. Mendive, T. Bredow, A. Feldhoff, M.A. Blesa, D. Bahnemann, Adsorption of oxalate on anatase (100) and rutile (110) surfaces in aqueous systems: Experimental results vs. theoretical predictions, Phys. Chem. Chem. Phys. 11 (2009) 1794. http://dx.doi.org/10.1039/B814608J

[8]   F. Roncaroli, M.A. Blesa, Kinetics of adsorption of carboxylic acids onto titanium dioxide, Phys. Chem. Chem. Phys. 12 (2010) 9938. http://dx.doi.org/10.1039/C003086D

[9]   F. Roncaroli, M.A. Blesa, Kinetics and equilibrium of surface complexation reactions: The adsorption of polycarboxylic acids on titanium dioxide, J. Coord. Chem. 63 (2010) 2488. http://dx.doi.org/10.1080/00958972.2010.487561

[10]   F. Roncaroli, M.A. Blesa, Kinetics of adsorption of oxalic acid on different titanium dioxide samples, J. Colloid Interf. Sci. 356 (2011) 227. http://dx.doi.org/10.1016/j.jcis.2010.11.051

[11]   F. Roncaroli, E.D. Martínez, G.J.A.A. Soler-Illia, M.A. Blesa, Mesoporous Thin Films of TiO2 on Attenuated Total Reflection Crystals. An In Situ Fourier-Transform Infrared Study of the Kinetics and Equilibrium of Adsorption and Photocatalysis of Carboxylic Acids, J. Phys. Chem. C 117 (2013) 15026. http://dx.doi.org/10.1021/jp312334y

[12]   A.D. Weisz, L. García Rodenas, P.J. Morando, A.E. Regazzoni, M.A. Blesa, FTIR study of the adsorption of single pollutants and mixtures of pollutants onto titanium dioxide in water: Oxalic and salicylic acids, Catal. Today 76 (2002) 103. http://dx.doi.org/10.1016/S0920-5861(02)00210-9

[13]   A.E. Regazzoni, P. Mandelbaum, M. Matsuyoshi, S. Schiller, S.A. Bilmes, M.A. Blesa, Adsorption and Photooxidation of Salicylic Acid on Titanium Dioxide: A Surface Complexation Description, Langmuir 14 (1998) 868. http://dx.doi.org/10.1021/la970665n

[14]   P.Z. Araujo, P.J. Morando, M.A. Blesa, Interaction of Catechol and Gallic Acid with Titanium Dioxide in Aqueous Suspensions. 1. Equilibrium Studies, Interaction of Catechol and Gallic Acid with Titanium Dioxide in Aqueous Suspensions. 1. Equilibrium Studies 21 (2005) 3470. http://dx.doi.org/10.1021/la0476985

[15]   P.Z. Araujo, P.J. Morando, E. Martínez, M.A. Blesa, Time evolution of surface speciation during heterogeneous photocatalysis: Gallic acid on titanium dioxide, Appl. Catal., B 125 (2012) 215. http://dx.doi.org/10.1016/j.apcatb.2012.05.035

[16]   P.Z. Araujo, V. Luca, P.B. Bozzano, H.L. Bianchi, G.J.d.A.v.A. Soler-Illia, M.A. Blesa, Aerosol-Assisted Production of Mesoporous Titania Microspheres with Enhanced Photocatalytic Activity: The Basis of an Improved Process, ACS Appl. Mater. Interfaces 2 (2010) 1663. http://dx.doi.org/10.1021/am100188q

[17]   P.V. Kamat, TiO2 Nanostructures: Recent Physical Chemistry Advances, J. Phys. Chem. C 116 (2012) 11849. http://dx.doi.org/10.1021/jp305026h

[18]   S. Eiden-Assmann, J. Widoniak, G. Maret, Synthesis and Characterization of Porous and Nonporous Monodisperse Colloidal TiO2 Particles, Chem. Mater. 16 (2003) 6. http://dx.doi.org/10.1021/cm0348949

[19]   L.-S. Zhong, J.-S. Hu, L.-J. Wan, W.-G. Song, Facile synthesis of nanoporous anatase spheres and their environmental applications, Chem. Commun. (2008) 1184. http://dx.doi.org/10.1039/B718300C

[20]   H.-G. Jung, C.S. Yoon, J. Prakash, Y.-K. Sun, Mesoporous Anatase TiO2 with High Surface Area and Controllable Pore Size by F−-Ion Doping: Applications for High-Power Li-Ion Battery Anode, J. Phys. Chem. C 113 (2009) 21258. http://dx.doi.org/10.1021/jp908719k

[21]   H.-E. Wang, J. Jin, Y. Cai, J.-M. Xu, D.-S. Chen, X.-F. Zheng, Z. Deng, Y. Li, I. Bello, B.-L. Su, Facile and fast synthesis of porous TiO2 spheres for use in lithium ion batteries, J. Colloid Interf. Sci. 417 (2014) 144. http://dx.doi.org/10.1016/j.jcis.2013.11.035

[22]   M. Estruga, C. Domingo, X. Domènech, J.A. Ayllón, Zirconium-doped and silicon-doped TiO2 photocatalysts synthesis from ionic-liquid-like precursors, J. Colloid Interf. Sci.
344 (2010) 327. http://dx.doi.org/10.1016/j.jcis.2009.12.063

[23]   P.C. Angelomé, G.J.D.A.A. Soler-Illia, Organically modified transition-metal oxide mesoporous thin films and xerogels, Chem. Mater. 17 (2005) 322. http://dx.doi.org/10.1021/cm048559b

[24]   G.L. Drisko, A. Zelcer, V. Luca, R.A. Caruso, G.J.D.A.A. Soler-Illia, One-pot synthesis of hierarchically structured ceramic monoliths with adjustable porosity, Chem. Mater. 22 (2010) 4379. http://dx.doi.org/10.1021/cm100764e

[25]   G.J.d.A.A. Soler-Illia, A. Louis, C. Sanchez, Synthesis and Characterization of Mesostructured Titania-Based Materials through Evaporation-Induced Self-Assembly, Chem. Mater. 14 (2002) 750. http://dx.doi.org/10.1021/cm011217a

[26]   G.J.D.A.A. Soler-Illia, C. Sanchez, B. Lebeau, J. Patarin, Chemical strategies to design textured materials: From microporous and mesoporous oxides to nanonetworks and hierarchical structures, Chem. Rev. 102 (2002) 4093. http://dx.doi.org/10.1021/cr0200062

[27]   G.L. Drisko, A. Zelcer, X. Wang, R.A. Caruso, G.J.D.A.A. Soler-Illia, Synthesis and photocatalytic activity of titania monoliths prepared with controlled macro- and mesopore structure, ACS Appl. Mater. Interfaces 4 (2012) 4123. http://dx.doi.org/10.1021/am300880q

[28]   P. Roonasi, A. Holmgren, An ATR-FTIR study of sulphate sorption on magnetite; rate of adsorption, surface speciation, and effect of calcium ions, J. Colloid Interf. Sci. 333 (2009) 27. http://dx.doi.org/10.1016/j.jcis.2008.12.080

[29]   J.L. Marco-Brown, M.M. Areco, R.M. Torres Sánchez, M. dos Santos Afonso, Adsorption of picloram herbicide on montmorillonite: Kinetic and equilibrium studies, Colloid. Surface A 449 (2014) http://dx.doi.org/121. 10.1016/j.colsurfa.2014.02.038

[30]   H.F. Krug, P. Wick, Nanotoxicology: An interdisciplinary challenge, Angew. Chem. Int. Ed. 50 (2011) 1260. http://dx.doi.org/10.1002/anie.201001037

[31]   J.H. Baxendale, N.K. Bridge, The photoreduction of some ferric compounds in aqueous solution, J. Phys. Chem. 59 (1955) 783. http://dx.doi.org/10.1021/j150530a022

[32]   N.I. Ermokhina, V.A. Nevinskiy, P.A. Manorik, V.G. Ilyin, V.N. Novichenko, M.M. Shcherbatiuk, D.O. Klymchuk, M.M. Tsyba, A.M. Puziy, Synthesis and characterization of thermally stable large-pore mesoporous nanocrystallineanatase, J. Solid State Chem. 200 (2013) 90. http://dx.doi.org/10.1016/j.jssc.2012.12.034

[33]   G.J.D.A.A. Soler-Illia, E. Scolan, A. Louis, P.A. Albouy, C. Sanchez, Design of meso-structured titanium oxo based hybrid organic-inorganic networks, New J. Chem. 25 (2001) 156. http://dx.doi.org/10.1039/B006139P

[34]   M. Thommes, B. Smarsly, M. Groenewolt, P.I. Ravikovitch, A.V. Neimark, Adsorption Hysteresis of Nitrogen and Argon in Pore Networks and Characterization of Novel Micro- and Mesoporous Silicas, Langmuir 22 (2005) 756. http://dx.doi.org/10.1021/la051686h

[35]   M. Kruk, M. Jaroniec, Argon adsorption at 77 K as a useful tool for the elucidation of pore connectivity in ordered materials with large cagelike mesopores, Chem. Mater. 15 (2003) 2942. http://dx.doi.org/10.1021/cm021774c

[36]   J. Rouquerol, F. Rouquerol, K.S.W. Sing, in: (Eds.), Adsorption by Powders and Porous Solids. Principles, Methodology and Applications; Academic Press, 24–28 Oval Road, London NW1 7DX, UK, 1999.

[37]   S.J.F. Herregods, M. Mertens, K. Van Havenbergh, G. Van Tendeloo, P. Cool, A. Buekenhoudt, V. Meynen, Controlling pore size and uniformity of mesoporous titania by early stage low temperature stabilization, J. Colloid Interf. Sci. 391 (2013) 36. http://dx.doi.org/10.1016/j.jcis.2012.07.098

[38]   E.L. Crepaldi, G.J.D.A.A. Soler-Illia, D. Grosso, F. Cagnol, F. Ribot, C. Sanchez, Controlled formation of highly organized mesoporous titania thin films: From mesostructured hybrids to mesoporous nanoanatase TiO2, J. Am. Chem. Soc. 125 (2003) 9770. http://dx.doi.org/10.1021/ja030070g

[39]   M.J. Henderson, A. Gibaud, J.F. Bardeau, J.W. White, An X-ray reflectivity study of evaporation-induced self-assembled titania-based films, J. Mater. Chem. 16 (2006) 2478. http://dx.doi.org/10.1039/B601677D

[40]   G.J.A.A. Soler-Illia, P.C. Angelomé, M.C. Fuertes, D. Grosso, C. Boissiere, Critical aspects in the production of periodically ordered mesoporous titania thin films, Nanoscale 4 (2012) 2549. http://dx.doi.org/10.1039/c2nr11817c

[41]   M. Haerifar, S. Azizian, Mixed surface reaction and diffusion-controlled kinetic model for adsorption at the solid/solution interface, J. Phys. Chem. 117 (2013) 8310. http://dx.doi.org/10.1021/jp401571m

[42]   M.M. Areco, L. Saleh-Medina, M.A. Trinelli, J.L. Marco-Brown, M. dos Santos Afonso, Adsorption of Cu(II), Zn(II), Cd(II) and Pb(II) by dead Avena fatua biomass and the effect of these metals on their growth, Colloid. Surface. B 110 (2013) 305. http://dx.doi.org/10.1016/j.colsurfb.2013.04.035

[43]   G. Blanchard, M. Maunaye, G. Martin, Removal of heavy metals from waters by means of natural zeolites, Water Res. 18 (1984) 1501. http://dx.doi.org/10.1016/0043-1354(84)90124-6

[44]   W. Rudzinski, W. Plazinski, Kinetics of Solute Adsorption at Solid/Solution Interfaces: A Theoretical Development of the Empirical Pseudo-First and Pseudo-Second Order Kinetic Rate Equations, Based on Applying the Statistical Rate Theory of Interfacial Transport, J. Phys. Chem. B 110 (2006) 16514. http://dx.doi.org/10.1021/jp061779n

[45]   J.Z. Guo, B. Li, L. Liu, K. Lv, Removal of methylene blue from aqueous solutions by chemically modified bamboo, Chemosphere 111 (2014) 225. http://dx.doi.org/10.1016/j.chemosphere.2014.03.118

[46]   G.E. Boyd, A.W. Adamson, L.S. Myers Jr, The exchange adsorption of ions from aqueous solutions by organic zeolites. II. Kinetics, J. Am. Chem. Soc. 69 (1947) 2836. http://dx.doi.org/10.1021/ja01203a066

[47]   X. Peng, F. Hu, J. Huang, Y. Wang, H. Dai, Z. Liu, Preparation of a graphitic ordered mesoporous carbon and its application in sorption of ciprofloxacin: Kinetics,

isotherm, adsorption mechanisms studies, Microporous Mesoporous Mater. 228 (2016) 196. http://dx.doi.org/10.1016/j.micromeso.2016.03.047

[48] S.J. Allen, G. McKay, K.Y.H. Khader, Intraparticle diffusion of a basic dye during adsorption onto sphagnum peat, Environ. Pollut. 56 (1989) 39. http://dx.doi.org/10.1016/0269-7491(89)90120-6

[49] Q. Sun, L. Yang, The adsorption of basic dyes from aqueous solution on modified peat–resin particle, Water Res. 37 (2003) 1535. http://dx.doi.org/10.1016/S0043-1354(02)00520-1

[50] M. Doğan, H. Abak, M. Alkan, Adsorption of methylene blue onto hazelnut shell: Kinetics, mechanism and activation parameters, J. Hazard. Mater. 164 (2009) 172. http://dx.doi.org/10.1016/j.jhazmat.2008.07.155

[51] L. Song, Y. Wang, L. Zhu, B. Guo, S. Chen, W. Wu, Surface modification to improve the sorption property of U(VI) on mesoporous silica, J. Radioanal. Nucl. Chem. 299 (2014) 1589. http://dx.doi.org/10.1007/s10967-014-2922-7

[52] N. Chen, Y. Li, D. Deng, X. Liu, X. Xing, X. Xiao, Y. Wang, Acetone sensing performances based on nanoporous TiO2 synthesized by a facile hydrothermal method, Sensor. Actuat. B Chem. 238 (2017) 491. http://dx.doi.org/10.1016/j.snb.2016.07.094

[53] M. Pelaez, N.T. Nolan, S.C. Pillai, M.K. Seery, P. Falaras, A.G. Kontos, P.S.M. Dunlop, J.W.J. Hamilton, J.A. Byrne, K. O'Shea, M.H. Entezari, D.D. Dionysiou, A review on the visible light active titanium dioxide photocatalysts for environmental applications, Appl. Catal., B 125 (2012) 331. http://dx.doi.org/10.1016/j.apcatb.2012.05.036

[54] R. Miao, Z. Luo, W. Zhong, S.Y. Chen, T. Jiang, B. Dutta, Y. Nasr, Y. Zhang, S.L. Suib, Mesoporous TiO2 modified with carbon quantum dots as a high-performance visible light photocatalyst, Appl. Catal., B 189 (2016) 26. http://dx.doi.org/10.1016/j.apcatb.2016.01.070